The receptor kinase FERONIA regulates phosphatidylserine localization at the cell surface to modulate ROP signaling

Marija Smokvarska, Vincent Bayle, Lilly Maneta-Peyret, Laetitia Fouillen,
Arthur Poitout, Armelle Dongois, Jean-Bernard Fiche, Julien Gronnier, José
Garcia, Herman Höfte, et al.

PLANT SCIENCES

The receptor kinase FERONIA regulates phosphatidylserine localization at the cell surface to modulate ROP signaling

Marija Smokvarska[1], Vincent Bayle[2], Lilly Maneta-Peyret[3], Laetitia Fouillen[3,4], Arthur Poitout[1], Armelle Dongois[1], Jean-Bernard Fiche[5], Julien Gronnier[6,7], José Garcia[1], Herman Höfte[8], Marcelo Nolmann[5], Cyril Zipfel[6,9], Christophe Maurel[1], Patrick Moreau[3], Yvon Jaillais[2], Alexandre Martiniere[1]*

Cells maintain a constant dialog between the extracellular matrix and their plasma membrane to fine tune signal transduction processes. We found that the receptor kinase FERONIA (FER), which is a proposed cell wall sensor, modulates phosphatidylserine plasma membrane accumulation and nano-organization, a key regulator of Rho GTPase signaling in Arabidopsis. We demonstrate that FER is required for both Rho-of-Plant 6 (ROP6) nano-partitioning at the membrane and downstream production of reactive oxygen species upon hyperosmotic stimulus. Genetic and pharmacological rescue experiments indicate that phosphatidylserine is required for a subset of, but not all, FER functions. Furthermore, application of FER ligand shows that its signaling controls both phosphatidylserine membrane localization and nanodomains formation, which, in turn, tunes ROP6 signaling. Together, we propose that a cell wall–sensing pathway controls via the regulation of membrane phospholipid content, the nano-organization of the plasma membrane, which is an essential cell acclimation to environmental perturbations.

INTRODUCTION

The coordination of plant growth and development needs a careful monitoring of environmental stimuli. Plant cells are under hydrostatic pressure (turgor) that maintains a tight association between the primary cell wall and the plasma membrane (PM). Change in water availability around the cell causes an osmotic signal that triggers short- and long-term plant responses. Despite their essential role for plant abiotic stress acclimation and also cell growth and division, how osmotic stimuli are perceived and transduced is just starting to be elucidated (1, 2).

One of the first cellular responses to hyperosmotic stress is an accumulation of reactive oxygen species (ROS) acting as secondary messengers for plant responses (3). Recently, we found that osmotically induced ROS accumulation requires the Rho-of-plants (ROP), ROP6, which acts upstream of the PM-localized RESPIRATORY BURST OXIDASE HOMOLOGUE (RBOH) D and F (4, 5). The osmotic signal targets within minutes ROP6 to specific nanodomains in the PM (5). Those ROP6-enriched nanodomains accumulate effector proteins like the RBOHs and are necessary and

sufficient to induce ROS in cells. Moreover, we found that the hyper variable tail of ROP6 interacts with anionic lipids (6). Among them, phoshatidylserine (PS) affects ROP6 retention time within nanodomains, which is critical for auxin signaling. The amount of PS in plant cells quantitatively regulates auxin-induced ROP signaling (6). Whereas lipid homeostasis is affected by the osmotic signal, the exact role of PS in this context remains at this stage unknown (7, 8).

The molecular mechanisms for osmotic signaling share similarities with the cell wall integrity (CWI) signaling pathway. This pathway transduces the cell wall status to the cell interior and coordinates multiple responses including cell elongation (9–11). Several of CWI sensors have been identified, and one of them called FERONIA (FER) has been extensively described to act in CWI maintenance upon environmental stresses (12). FER belongs to the *Catharanthus roseus* receptor-like kinase (CrRLK1L) family and was associated with a variety of cellular processes, from the preservation of cell integrity in tip-growing cells and root elongation, to response to biotic and abiotic stress (13–25). Loss of FER function reduces the level of activated ROPs and hampers ROP-mediated and RBOH-dependent ROS production (14, 26). The mechanism by which FER perceives the cell wall status remains however to be determined. FER can bind pectin through the two tandem malectin-like domain in its extracellular part, (18, 24, 27). In addition, the FER ectodomain binds secreted RAPID ALKALIZATION FACTOR (RALFs) peptides (16, 17, 28, 29). Structural and biochemical studies demonstrated that RALFs bind to FER, together with LORELEI (LRE)–LIKE GLYCOSYLPHOSPHATIDYLINOSITOL (GPI)–ANCHORED PROTEINs (LLGs) (28, 30–32). In addition, RALFs bind with nanomolar affinities to LRR extensins (LRXs), a class of protein associated with the cell wall (19, 20, 28, 33).

[1]IPSiM Univ Montpellier, CNRS, INRAE, Institut Agro, Montpellier, France. [2]Laboratoire Reproduction et Développement des Plantes, Univ Lyon, ENS de Lyon, UCB Lyon 1, CNRS, INRA, F-69342 Lyon, France. [3]UMR 5200 Membrane Biogenesis Laboratory, CNRS and University of Bordeaux, INRAE Bordeaux, Villenave d'Ornon, France. [4]MetaboHub-Bordeaux, Metabolome platform, INRAE, Villenave d'Ornon, France. [5]Centre de Biochimie Structurale, Centre National de la Recherche Scientifique Unité Mixte de Recherche 5048, Institut National de la Santé et de la Recherche Médicale U1054, Université de Montpellier, 34090 Montpellier, France. [6]Institute of Plant and Microbial Biology and Zurich-Basel Plant Science Center, University of Zurich, 8008 Zurich, Switzerland. [7]University of Tübingen, Center for Plant Molecular Biology (ZMBP), 72076 Tübingen, Germany. [8]Université Paris-Saclay, INRAE, AgroParisTech, Institut Jean-Pierre Bourgin (IJPB), 78000, Versailles, France. [9]The Sainsbury Laboratory, University of East Anglia, Norwich Research Park, NR4 7UH, Norwich, UK.
*Corresponding author. Email: alexandre.martiniere@cnrs.fr

Under hyperosmotic stimulation, the cell wall deforms and, in extreme cases, can be dissociated from the PM. The partial or complete loss of the interaction with the PM has a large effect on the wall and wall-associated proteins, which are anchored to the PM and are important for maintaining cell wall function. Because of this, and the fact that FER induces ROS production through the activation of small guanosine triphosphatases (GTPases) (14, 26), we hypothesized that FER constitutes an interesting candidate for osmotic perception and the downstream activation of the small GTPase ROP6. In most instances, Rho GTPases are activated by receptor kinases and thus act downstream in the signaling cascade.

By contrast, we found that FER acts independently of ROP6 activation during osmotic sensing. Further analysis revealed that FER regulates ROP6 signaling rather indirectly by controlling the organization and localization of the anionic lipid, phosphatidylserine (PS) at the PM.

RESULTS

FER is required for osmotic signaling but not through ROP6 activation

To determine whether FER is involved in osmotic stress signaling, we used cellular ROS accumulation as a fast phenotypic output and tested the phenotypes of independent FER alleles: *fer-4*, a knockout allele, and *fer-5,* a knockdown mutant (14, 34). The *fer-5* mutation produces a truncated RNA lacking part of the kinase domain and milder growth phenotype compared to the knockout allele (14). Compared to Col-0, both *fer-4* and *fer-5* showed insensitivity to the hyperosmotic treatment induced by dipping plantlets in a 300 mM sorbitol solution (with thereby a low water potential: ψ = −0.75 MPa) for 15 min (Fig. 1, A and B). To further confirm the role of FER in osmotic signaling, we tested the effects of treatment with RALF23 peptide, a well described ligand of FER that negatively regulates FER function in several signaling contexts (17, 19, 28, 35). Sixty minutes RALF23 pretreatment showed an inhibitory effect on osmotically induced ROS production (Fig. 1C). This inhibitory effect of RALF23 is reminiscent of microbe-associated molecular pattern-induced ROS production (fig. S1A) (17, 28, 35).

We recently showed that the small GTPase ROP6 is required for osmotically induced ROS accumulation in roots (5). Thus, we hypothesized that FER, being a receptor kinase, might activate ROP6 during this signaling event. To test this hypothesis, we took advantage of plants expressing a genomic GTP-locked version of ROP6 under the control of its native promoter (mCit-ROP6gCA). This line was previously shown to display a constitutive ROS accumulation independent from osmotic stimulation (Fig. 1D) (5). Both knockdown and knockout alleles of *FER* inhibited the mCit-ROP6gCA phenotype (Fig. 1D). Furthermore, pretreatment with RALF23 peptide inhibited the constitutive ROS production of the mCit-ROP6gCA line (Fig. 1E). These results suggest that FER may act on ROP6 signaling independently of its activation and confirm that 60 min of RALF23 treatment negatively regulates this pathway. Since FER was reported to modulate both splicing and translation of *ROP* mRNAs (36, 37), we verified the mCit-ROP6gCA protein levels using immunoblotting and did not observe any differences between wild-type (WT), *fer-4*, or *fer-5* backgrounds that could explain their respective ROS defects (fig. 1SB). Next, we checked whether mCit-ROP6g-CA could be mislocalized in *fer* mutants. Although the signal of mCit-ROP6g-CA was

higher in *fer-5* than in *fer-4* or WT, the ratio between PM and intracellular labeling was the same between all genotypes (fig. S1, C to E). Consequently, we did not observe drastic changes in protein quantity or PM targeting that could explain the suppression of the GTP-locked ROP6 phenotype in the different *fer* mutants.

The FER pathway affects the PM localization of PS

Since we did not observe an obvious mislocalization of mCit-ROP6g-CA in *fer* mutants (Fig. 1, C to E), we hypothesized that FER might regulate the spatial distribution and/or dynamics within the PM of ROP6, given the propensity of activated ROP6 to accumulate in PS-enriched nanodomains (6). To reveal a potential link between ROP6-containing nanodomains, PS and FER, we first tested the role of PS during osmotic signaling in plants with varying PS levels: the loss-of-function mutant *phosphatidylserine synthase* (*pss)1-3,* which totally lacks PS, and the transgenic line overexpressing *PSS1* (PSS1ox1), which shows a two-third increase in PS relative to WT Col-0. We observed no osmotically induced ROS accumulation in *pss1-3* and no further increase in ROS levels in PSS1ox1 relative to Col-0 (Fig. 2A) (38). This suggests that PS is required but not a limiting factor for osmotic signaling pathway (Fig. 2A).

We next wondered whether the FER loss-of-function phenotype (Fig. 1B) might reflect possible changes in PS levels. Lipid quantification by high-performance thin layer chromatography (HPTLC) showed that Col-0, *fer-4*, and *fer-5* had similar lipid profiles, except for triacylglycerols, which are less abundant in the mutant lines (fig. S2A). Regarding the phospholipids, no differences in PS quantity was found between the different genotypes (Fig. 2B). *fer-4,* only, show a small increase in quantity of phosphatidylcholine (PC) and phosphatidylethanolamine (PE) (Fig. 2B). Since the PS quantity was not altered in *fer* mutants, we next wonder whether PS quality might change. The fatty acyl chains of PS are known to vary a lot in terms of its length and saturation. Again, no clear differences were found (fig. S2B). Together, these results show that *fer* mutations had only limited effects on the quantity and the profile of tested lipids.

Since the total quantity of PS was not affected in *fer* mutants, we next asked whether FER controls the subcellular distribution of PS. PS is known to partition between the PM and endosomes, a phenomenon that is dynamically regulated during root development (6, 38). This dual localization of PS was previously reported using two independent PS biosensors, 2PH[EVECTIN] and C2[LACT] (38, 39). It should be noted that although PS is required for the localization of both sensors, 2PH[EVECTIN] has a lower affinity for the PM than C2[LACT] (38). This was also observed in yeast and animal cells, but the exact reason for this difference is unknown (40, 41). Furthermore, in plants, both sensors show a consistently higher PM localization in the apical meristem relative to elongating or auxin-treated cells (6). We generated independent lines by crossing both sensors with *fer-4* and *fer-5* mutants to analyze the potential role of FER in PS distribution. We observed a lower PM signal for both sensors in the two *fer* mutant alleles relative to Col-0 (Fig. 2, C to F). This effect was not observed in *rop6-2* confirming that ROP6 does not control PS localization at the PM (fig. S3, A to C). Then, by exogenous application of RALF23, we investigated whether activation of the FER pathway could modify PS localization. RALF23 induced an accumulation of PS biosensors at the PM after 15 min of treatment (Fig. 3, A to D). However, this increase was transient since, at later time points, RALF23 treatment decreased the relative signal
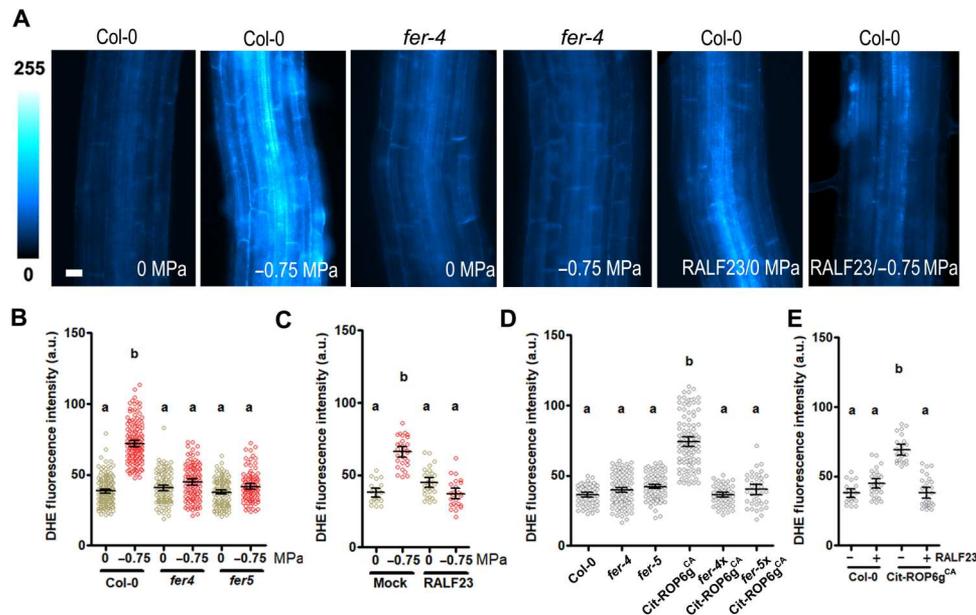
Fig. 1. FER signaling pathway is necessary to trigger osmotically induced ROS accumulation independently of ROP6 activation. (**A**) Images of dihydroethidium (DHE) stained root cells of Col-0, the FER knockout allele (*fer-4*), and knockdown allele (*fer-5*) in control conditions (0 MPa) or after 15 min of a −0.75-MPa treatment in the presence or absence of the FER ligand RALF23. (**B**) DHE fluorescence quantification after a 15-min treatment with a control or −0.75-MPa solution of the different genetic materials. (**C**) DHE fluorescence quantification of Col-0 pretreated with 1 μM RALF23 for 60 min followed by a control (0 MPa) or −0.75-MPa treatment for 15 min. (**D**) DHE fluorescence quantification in *fer-4* and *fer-5*, in a line expressing auto-active genomic DNA of ROP6 (mCit-ROP6gCA) and in the corresponding crosses (*fer-4*xmCit-ROP6gCA and *fer-5*xmCit-ROP6gCA). (**E**) ROS quantification from DHE fluorescence signal after treatment with a 1 μM RALF23 peptide for 60 min on Col-0 and mCit-ROP6gCA [Col-0 data are replotted from (C)]. Error bars correspond to the 95% confidence interval. According to analysis of variance (ANOVA) followed by a Tukey test, letters indicate significant differences among means ($P < 0.01$). $n > 26$ cells from three to five independent biological replica. Scale bar, 10 μm. a.u., arbitrary units.

of PS biosensors at the PM (Fig. 3, A to D). Both short-term induction (15 min) and long-term inhibition (60 min) of PS PM-localization were abolished in *fer-4*, demonstrating that functional FER is required for PS delocalization after RALF23 treatment (Fig. 3, E and F).

Next, we wondered what the impact of RALF23 short-term on osmotically induced ROS accumulation could be. Whereas 60 min of RALF23 pretreatment recapitulated the inhibition of osmotically induced ROS accumulation, a short treatment (15 min) revealed a strong enhancement of ROS signal in cells (Fig. 3G). This observation underlines the correlation between PS localization at the PM and osmotically induced ROS production.

FER signaling controls PS nanodomain formation

Our results suggest that the FER pathway controls PS quantity and/ or availability at the PM. We thus wondered whether it could also control its nanodomain distribution at the PM, since PS nanodomain formation is required for ROP6 signaling (6). PS nanodomains are not resolvable with confocal setup, therefore we applied total internal reflection fluorescence (TIRF) microscopy on Col-0– and *fer-4*–expressing C2^{LACT}. This PS biosensor was used as it gives the strongest signal at the PM (6). The C2^{LACT} dotted structures, previously described as PS nanodomains (6), were present in Col-0 but mostly absent in *fer-4*, and the density of C2^{LACT} clusters did not change upon osmotic stimulation (Fig. 4, A and B). Furthermore, we found that after a long-term treatment (60 min), the density of C2^{LACT} clusters decreased, thus mimicking the *fer-4* phenotype (Fig. 4, B and C). These results suggest that FER signaling

can modulate the number of PS nanodomains at the PM, independently of the osmotic signal, disconnecting FER and osmotic signaling pathways.

FER signaling acts on ROP6 clustering and dynamics in the PM

Since PS is required for ROP6 nanodomain formation (5, 6), we analyzed green fluorescent protein (GFP)–ROP6 localization using TIRF. As previously reported, the GFP-ROP6 signal in osmotically induced cells appeared as diffraction-limited spots (fig. S4A) (5). The *fer-4* mutation did not affect the density of GFP-ROP6 nanodomains as compared to WT Col-0 (fig. S4, A and B). Unexpectedly, this shows that in the absence of FER, ROP6 nanodomains were still formed. However, we previously showed that the depletion of PS in *pss1-3* is not preventing ROP6 nanodomains formation. It rather disrupts ROP6 dynamics within those domains, e.g., exchanges in/out of nanodomains (6).

To determine ROP6 dynamics, we took advantage of single-particle tracking photoactivated localization microscopy (sptPALM), a superresolution method that allows the diffusion coefficient of tens of thousands of molecules to be estimated in living cells (42, 43). As we previously reported (5), the distribution of the instantaneous diffusion coefficient of single ROP6 molecules extrapolated from mean square displacement plots was bimodal (Fig. 4, D and E; highly and poorly diffusible molecules in yellow and blue, respectively). Diffusible ($D_{diff} = 0.05$ μm/s^{-2}) and relatively immobile ($D_{imm} = 0.0007$ μm/s^{-2}) mEOS2-ROP6 coexisted within the PM. Minutes after an osmotic treatment, the proportion of immobile molecules increased
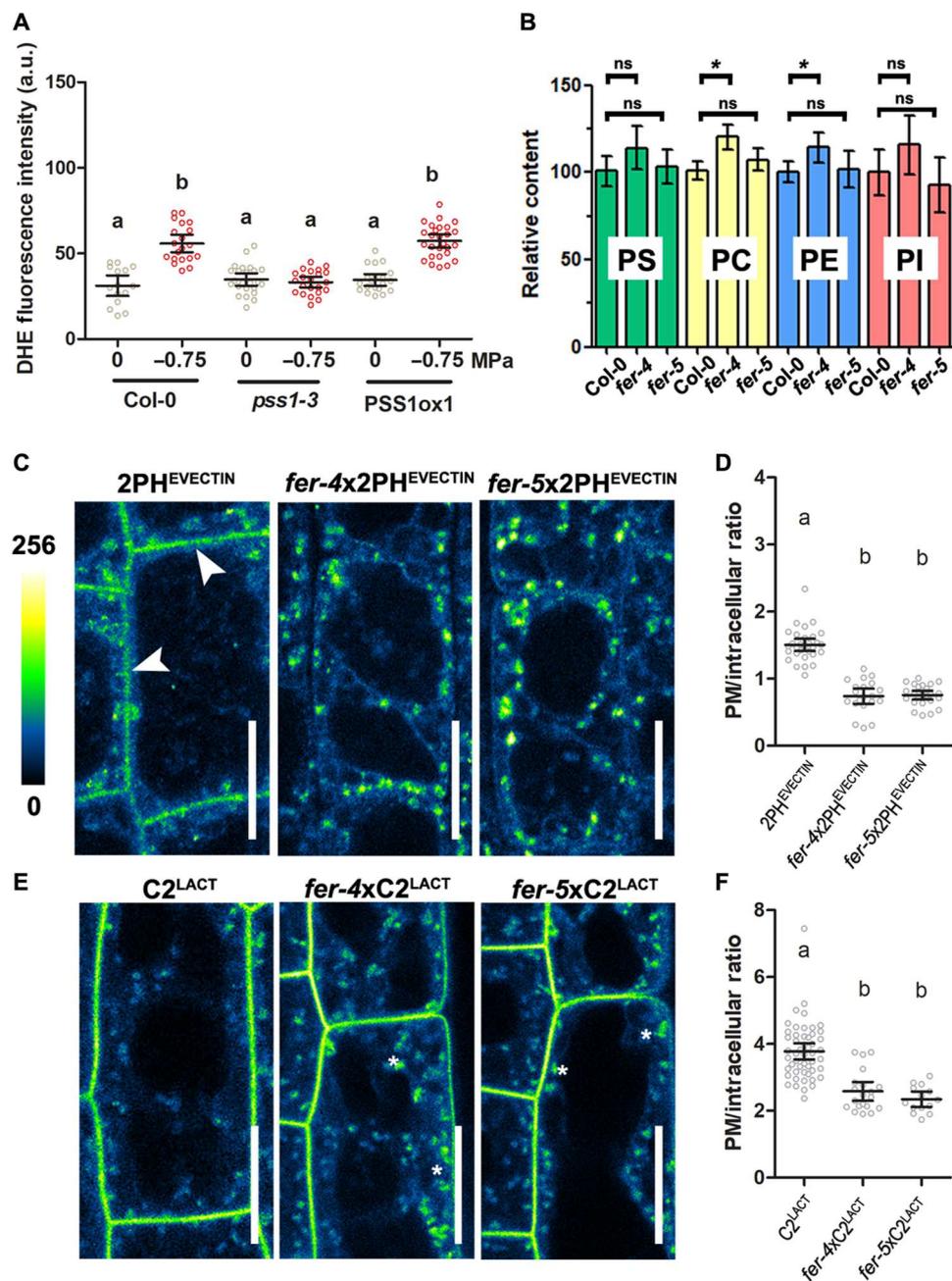
Fig. 2. FER regulates PS PM localization. (**A**) DHE fluorescence quantification of Col-0, *pss1-3*, and PSS1ox1 overexpressing line, in control condition or after an osmotic stimulation (−0.75 MPa). (**B**) Quantification of the PS, PC, PE, and PI by HPTLC in Col-0, *fer-4*, and *fer-5*. *fer-4* and *fer-5* values are shown as relative content compared to Col-0. Confocal micrograph showing the localization of the two PS biosensors 2PH^EVECTIN (**C**) and C2^LACT (**E**) in Col-0, *fer-4*, or *fer-5* and their respective PM/intracellular ratio quantification (**D** and **F**). Arrowheads show PM labeling and stars enhanced staining of the trans-Golgi network (TGN). Error bars correspond to the 95% confidence interval. According to ANOVA followed by Tukey test, letters indicate significant differences among means ($P < 0.01$). In (B), a paired Wilcoxon test was done comparing *fer-4* to Col-0 and *fer-5* to Col-0 for each lipid separately. * $P < 0.05$ For (B), $n > 7$; for (C), $n = 3$; and for (A), (E), and (F), $n > 14$ from at least two independent biological replicates. Scale bars, 20 μm. ns, not significant.

almost twofold (Fig. 4, E and F). In *fer-4*, this effect was abolished, suggesting that at the nanometric scale, independently of osmotic stimulation, mEOS2-ROP6 always diffuses similarly than in untreated cells (Fig. 4, D to F). Vonoroï segmentation estimated that nanodomain size and density in the PM and the relative occurrence of mEOS2-ROP6 within nanodomains were not affected in *fer-4*

mutant (Fig. 4, G to J). These single molecule data using mEOS2-ROP6 are in accordance with our TIRF experiments on GFP-ROP6 (fig. S4, A and B). Together, our analyses indicate that in a *fer-4* background, ROP6 nanodomains are still formed, but ROP6 is not immobilized upon osmotic treatment as it is in a WT background. This effect is similar to the one previously described in
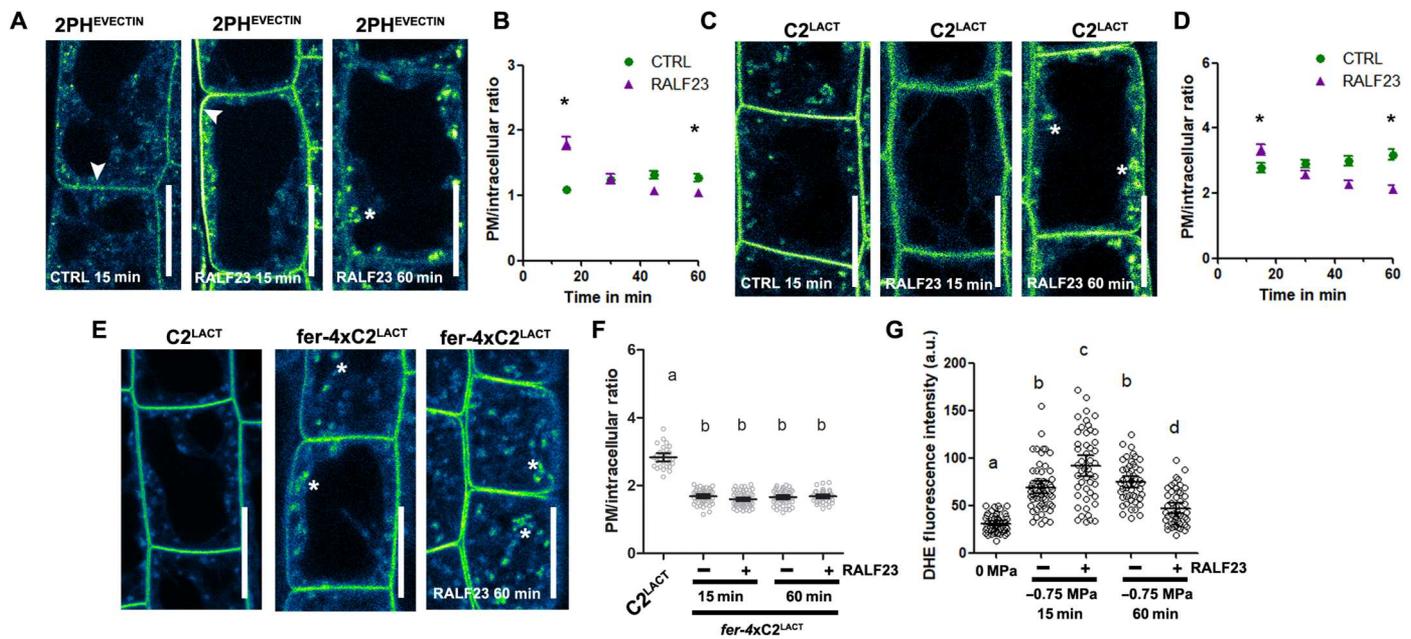
Fig. 3. RALF23/FER induces a transient accumulation of PS at the PM. Confocal micrograph showing the localization of the two PS biosensors 2PH[EVECTIN] (**A**) and C2[LACT] (**C**) along 1 μM RALF23 treatment and their respective quantification (**B** and **D**). (E) Confocal micrograph of fer-4xC2[LACT] after RALF23 treatment and its PM/intracellular ratio quantification (**F**). (**G**) DHE fluorescence quantification of Col-0 plants in the presence or absence of osmotic stimulation (−0.75 MPa) with or without RALF23 pretreatment. Error bars correspond to the 95% confidence interval. According to ANOVA followed by Tukey test, letters indicate significant differences among means ($P < 0.01$). For (B) and (D), at 15 and 60 min, t test was used for comparison between control and RALF23 treated plants. * $P < 0.05$, $n > 15$ from three independent biological replicates. Scale bars, 10 μm.

pss1-3 (6), suggesting that the impact of the FER pathway on PS cellular distribution might regulate ROP6 dynamics and signaling.

To confirm the role of FER on ROP6 clustering and dynamics, we took advantage of the transient effect of RALF23 treatment on both PS localization and ROS signaling (Fig. 3, B, D, and G). First, we analyzed GFP-ROP6 localization using TIRF after a short- or long-term RALF23 pretreatment followed by an osmotic stimulation. As anticipated, RALF23 had an inhibitory effect on GFP-ROP6 cluster density after long-term treatment; this effect being FER dependent (fig. S4, A, C, D, and E). Unexpectedly, a similar result was obtained with short-term RALF23 treatment, where ROS signaling was enhanced. However, as previously described, GFP-ROP6 clusters are too small to be properly resolved by conventional light microscopy (5, 6). Therefore, to get a more precise insight into the clustering and dynamic of ROP6 molecules, we used sptPALM experiments. Pretreatment with RALF23 for 15 min increased the immobile fraction of mEOS2-ROP6 molecules only after osmotic stimulation (Fig. 5, A to D). Next, we wondered how this drastic change in ROP6 dynamic affects ROP6 clustering. Voronoi segmentation revealed that short-term treatment with RALF23 enhances the relative number of mEOS2-ROP6 molecules in nanodomains, without affecting nanodomains density or size (Fig. 5, E to H). Thus, RALF23 short-term treatment not only led to higher ROS accumulation after osmotic cell stimulation but also enhanced the recruitment and immobilization of ROP6 molecules in nanodomains. By contrast, long-term RAFL23 treatment decreased ROP6 nanodomain size, density, and the relative occurrence of mEOS2-ROP6 within nanodomains, without affecting mEOS2-ROP6 diffusion (Fig. 5, D and F to H). Those results showed that although ROP6 molecules are still getting immobilized

after an osmotic stimulation, they failed to cluster in nanodomains, likely because PS nanodomains are missing in the membrane after long-term RALF23 treatment (Fig. 4C). However, GFP-RBOHD clustering was not affected by RALF23 pretreatment (fig. S4, F and G), suggesting that the FER-RALF23 pathway does not have a general effect on PM protein dynamics.

Our observations show that FER acts on PS cellular distribution and nano-organization at the PM. PS is required for ROP6 dynamics and function (Fig. 2A) (6). Furthermore, the effects of RALF23 treatment on PS localization correlate with those on ROP6 dynamics and osmotically induced ROS production. Thus, our results are consistent with a model in which FER-dependent regulation of PS distribution tunes ROP6 dynamics at the PM and thereby its downstream signaling output.

Regulation of PS localization and nanodomain formation act downstream of FER signaling pathway

To determine whether the defects in PM/trans-Golgi network (TGN) PS localization or PS nanodomain formation of FER loss-of-function plants are limiting, we carried out complementation assays with exogenous application of lysophospholipids. They are more soluble than phospholipids and hence more likely to reach the cytosolic leaflet of cellular membranes (44, 45). This approach has already been proven functional: Short-term (i.e., 1 hour) treatment with Lyso-PS could rescue the membrane localization of a PS sensor in the pss1 mutant, and long-term treatment could reverse part of the pss1-3 root developmental phenotype (38). Roots of fer-4x2PH[EVECTIN] supplemented for 1 hour with Lyso-PS (Fig. 6, A and B) showed a relocalization of 2PH[EVECTIN] back to the PM, making them similar to WT plants. Identical results were found
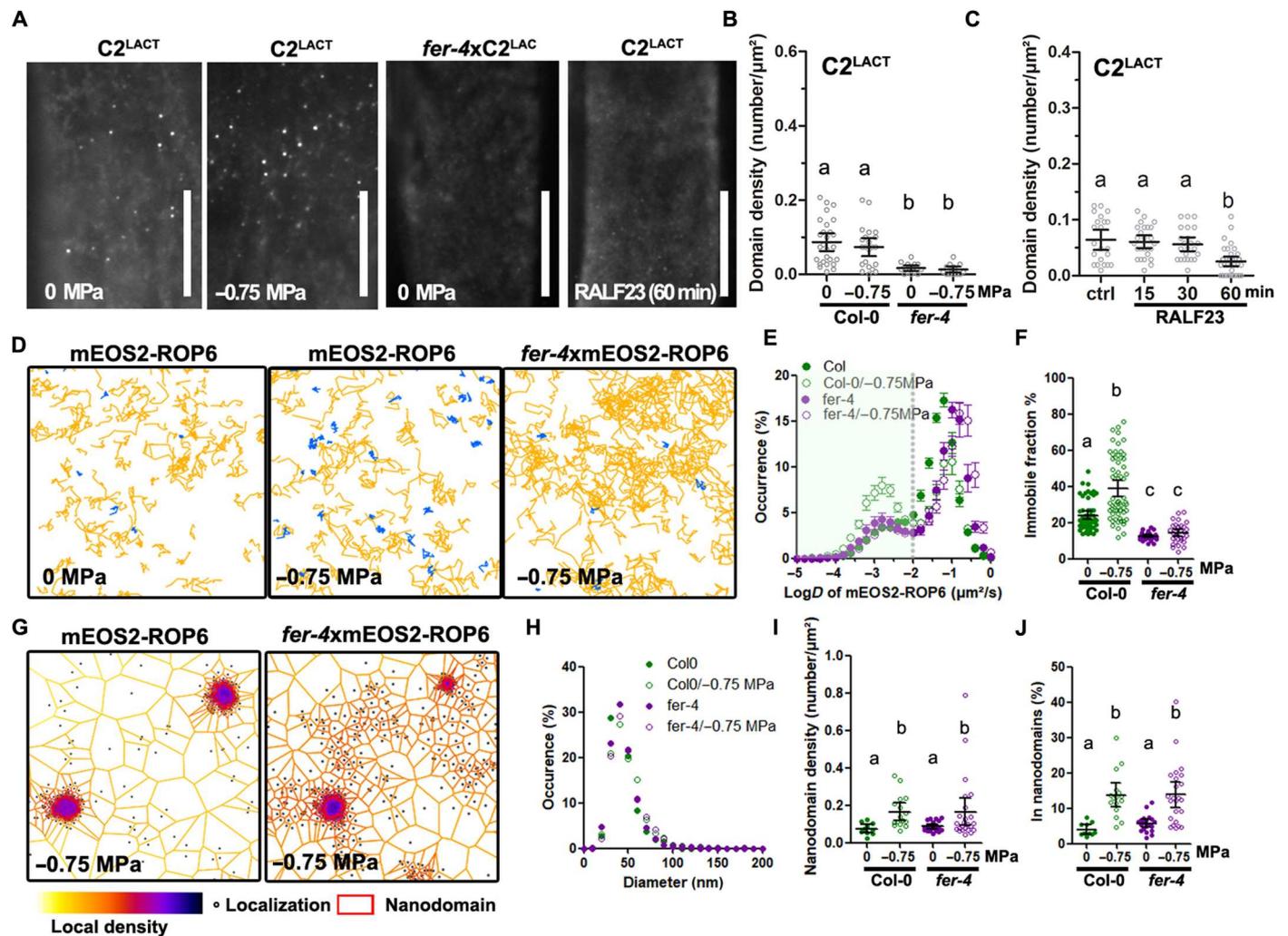
Fig. 4. FER regulates PS nanodomains density and ROP6 dynamics. (**A**) TIRFM micrograph of C2^{LACT} and *fer-4*xC2^{LACT} in control conditions or after 1 μM RALF23 treatment. (**B**) and (**C**) correspond to the cluster density quantification. (**D**) Image reconstruction of several tens of single mEOS2-ROP6 molecule trajectories from either Col-0 or *fer-4* plants in control conditions or after 2 min of a −0.75-MPa treatment. Trajectories with low or high instantaneous diffusion coefficient are labeled in blue and yellow, respectively. (**E**) Bimodal distribution of molecule instantaneous diffusion coefficient in control or after osmotic stimulation (open symbol) for plants expressing mEOS2-ROP6 in Col-0 or *fer-4*. (**F**) Histogram represents the percentage of molecules with an instantaneous diffusion coefficient below 0.01 μm² s⁻¹ in control conditions or after hyperosmotic treatment. (**G**) Vonoroï tessellation of mEOS2-ROP6 molecule localization map in Col-0 or *fer-4* under hyperosmotic treatment. Color code represents the local density of each molecule (labeled as a black circle). Nanodomains are highlighted by a red circle. (**H**) Distribution of nanodomain diameters. (**I**) Nanodomain density and (**J**) relative occurrence of mEOS2-ROP6 in nanodomains in control or after treatments for Col-0 or *fer-4* plants. Error bars correspond to the 95% confidence interval. ANOVA followed by Tukey test, letters indicate significant differences among means ($P < 0.01$). $n > 26$ from at least two independent biological replica. Scale bars, 10 μm

for the knockdown allele *fer-5* (fig. S5, A and B). Plants supplemented with Lyso-PA did not allow such relocalization of the PS biosensor in *fer-4* and *fer-5*, although the Lyso-PA treatment was functional in our experimental condition as it complemented the PM localization of the PA biosensor (2xPASS) after inhibition of phospholipase D activity by 5-fluoro-2-indolyl des-chlorohalopemide (FIPI) treatment (Fig. 6, A and B, and fig. S5, A to C). In addition, TIRF observation revealed that Lyso-PS can also restore C2^{LACT} nanodomains clustering in *fer-4* (Fig. 6, C and D).

Since Lyso-PS can complement 2PH^{EVECTIN} localization in *fer* mutants, we wondered whether it could rescue osmotic signaling pathway. ROS accumulation in roots was quantified in Col-0, *fer-*

4, and *fer-5* after osmotic stimulation in the presence or absence of Lyso-PS in the media. Exogenous addition of Lyso-PS complemented the osmotically induced ROS accumulation in *fer-5* and partially in *fer-4* (Fig. 6E), whereas Lyso-PA had no effect (fig. S5D). To confirm the role of PS in osmotically mediated ROS accumulation, we generated crosses between the two independent mutant alleles of FER and PSS1ox1. In those genetic background, PSS1ox1 restored a WT ROS response to osmotic treatment in both mutants (Fig. 6F). In conclusion, both exogenous supply or genetic modulation of PS quantity can overcome the loss of FER function in plants, with respect to osmotic signaling.
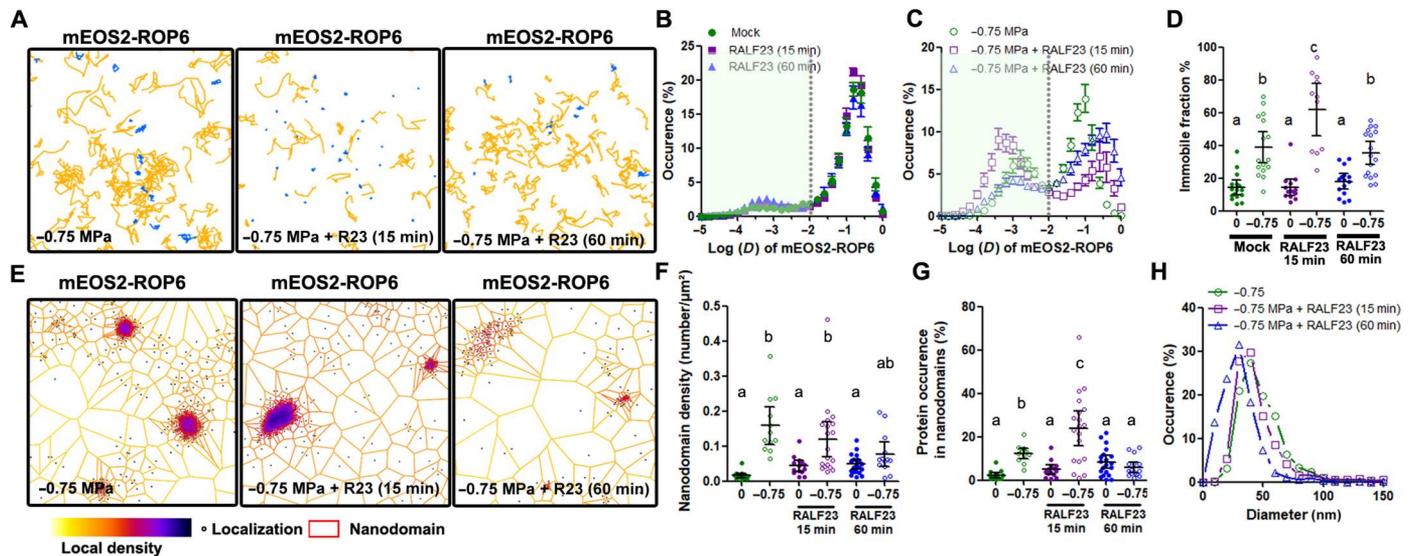
Fig. 5. RALF23/FER acts both on ROP6 diffusion and clustering. (**A**) Image reconstruction of several tens of single mEOS2-ROP6 molecule trajectories after RALF23 pretreatment of 15 or 60 min and followed by osmotic stimulation. Trajectories with low or high instantaneous diffusion coefficient are labeled in blue and yellow, respectively. Bimodal distribution of molecule instantaneous diffusion coefficient in control (**B**) or after osmotic stimulation (**C**) for plants expressing mEOS2-ROP6 in the absence (green circle), 15-min (purple squared), or 60-min RALF23 pretreatment (blue triangle). (**D**) Histogram represents the percentage of molecules with an instantaneous diffusion coefficient below 0.01 $\mu m^2 s^{-1}$. (**E**) Vonoroï tessellation of mEOS2-ROP6 molecule localization map after RALF23 pretreatment of 15 or 60 min and followed by osmotic stimulation. Color code represents the local density of each molecule (labeled as a black circle). Nanodomains are highlighted by a red circle. (**F**) Nanodomain density and (**G**) relative occurrence of mEOS2-ROP6 in nanodomains after RALF23 pretreatment of 15 or 60 min followed by osmotic stimulation. (**H**) Distribution of nanodomain diameters. Error bars correspond to the 95% confidence interval. ANOVA followed by Tukey test, letters indicate significant differences among means ($P < 0.01$). $n > 12$ from at least two independent biological replica.

Then, we wondered whether Lyso-PS treatment could act on ROP6 activation. To do so, we compared ROS accumulation in mCit-ROP6gCA and *fer-4*xmCit-ROP6gCA lines. Exogenous Lyso-PS restored WT ROS levels in *fer-4*xmCit-ROP6gCA even in the absence of the osmotic signal (Fig. 6G). In contrast, the loss of osmotically induced ROS accumulation present in *rop6-2* could not be reverted by Lyso-PS treatment (Fig. 6E). These data point that in *fer* mutants, PS is a limiting factor for ROP signaling.

All these data show that FER can control protein dynamics at the PM by acting on lipid organization that is later required for ROS signaling. Next, we tested whether this could also control other ROS-related signaling pathways downstream of FER. The FER pathway is known to control PAMP triggered immunity (PTI) signaling in plants by regulating ligand-binding receptor complexes at the PM (fig. S1A), such as FLS2-BAK1 complex formation induced in response to the bacterial elicitor (flg22) (*17*, *28*, *35*). In agreement with this model, FER loss-of-function plants presented a reduced ROS accumulation after flg22 treatment (fig. S6, A and D). However, both pharmacological and genetic complementation assays with Lyso-PS and PSS1ox1, respectively, failed to complement flg22-triggered extracellular ROS accumulation in leaf discs (fig. S6, A to D). This result prompted us to explore more broadly FER-dependent phenotypes in non-root tissues. Recently, FER and ROPs were associated with cell polarity in leaves (*14*, *24*, *27*, *46*). FER loss-of-function mutants, but also multiple mutants of ROPs, were reported to have disrupted pavement cell shape, resulting in less lobed cells (*27*, *47*). A similar phenotype was described for the PS biosynthesis mutant *pss1-3* (*6*). By growing *fer-4* seedlings for 3 days on media containing Lyso-PS, we observed restoration of

normal pavement cell shapes with indentations and lobes (Fig. 6, H and I). This rescue of pavement cell shape was also found in cotyledons of the *fer-4*xPSS1ox1 line, but not upon Lyso-PA treatment in *fer-4* (Fig. 6, H and J, and fig. S6, E and F). This is associated to a rescue of the cotyledon growth defect (fig. S6, G and H). Last, we tested other *fer-4* related phenotypes. While root gravitropic response was partially restored, auxin-induced root hair elongation was not (fig. S6, I to K). Together, this set of results shows that the regulation of PS localization by FER is a determinant for only a subset of FER-dependent functions.

DISCUSSION
FER participates in a plethora of signaling pathways involved in plant development, reproduction, and environmental interactions (*12*, *48*). For instance, FER controls auxin-induced root hair growth (*14*), abscisic acid (ABA)-induced guard cell turgor regulation (*49*), or pathogen response in leaves (*17*, *50*). In this last example, FER controls the dynamics of the flagellin receptor FLS2 and its coreceptor BAK1 and consequently their complex formation (*17*, *35*). Our results uncover a new function for FER, showing that it acts on the strength of the osmotically induced ROS accumulation (Fig. 3G). This mechanism is regulated by PM/TGN PS localization and/or nanodomains density at the PM, which is later acting as platforms for ROP6 signaling (Figs. 4 and 5 and fig. S4). Thus, FER is a necessary, but not sufficient, modulator of the osmotic signaling, since the quantity of PS nanodomains at the PM is not regulated by the osmotic signal per se (Fig. 4B).
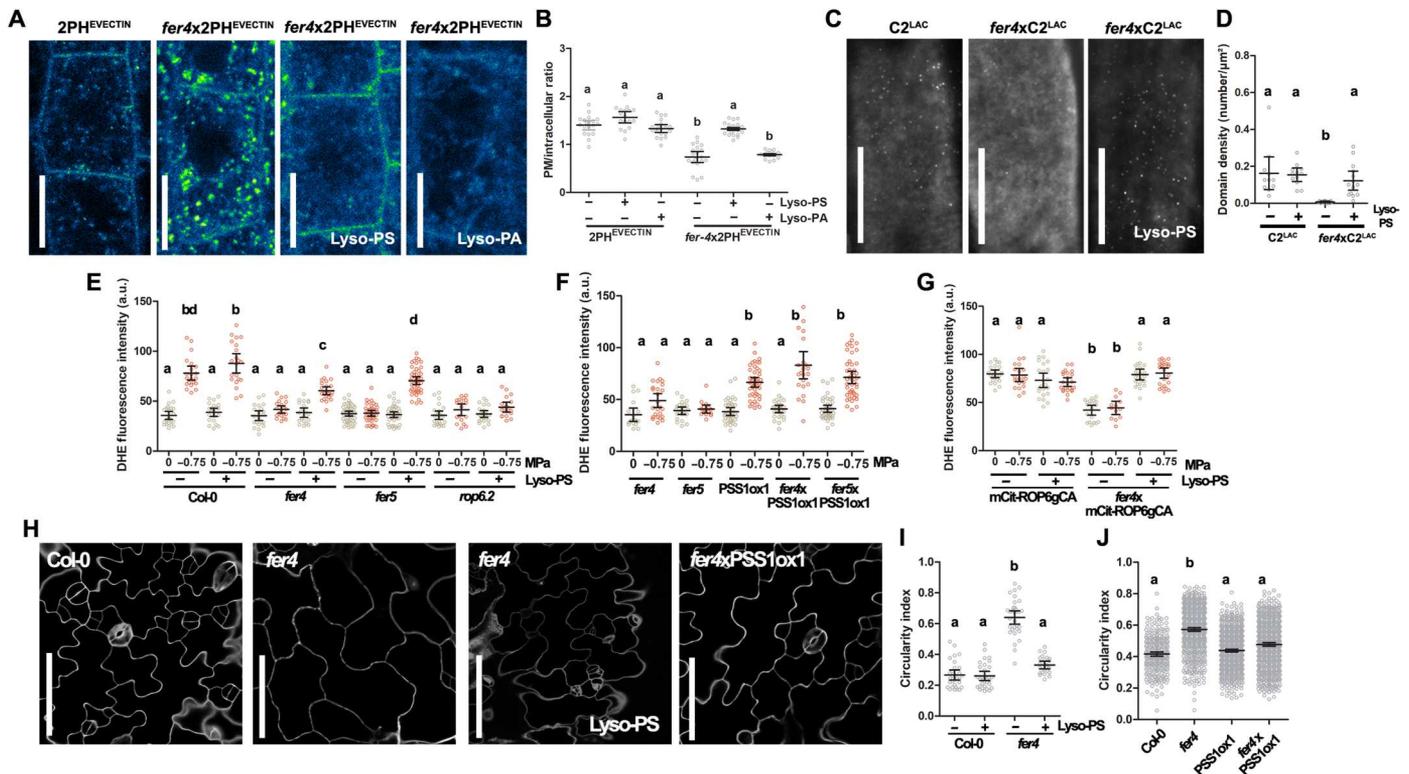
Fig. 6. Genetic overexpression or exogenous addition of Lyso-PS, but not Lyso-PA reverse *FER* loss of function phenotypes. (**A**) Confocal micrograph showing the localization of the PS biosensors 2PH^{EVECTIN} in Col-0 or *fer-4* background with or without 1 hour of Lyso-PS or Lyso-PA and corresponding quantification of the PM/intracellular ratio (**B**). (**C**) TIRFM micrograph of C2^{LACT} and *fer-4*xC2^{LACT} supplemented or not with Lyso-PS and corresponding cluster density quantification (**D**). (**E**) DHE fluorescence quantification in Col-0, *fer-4*, *fer-5*, and *rop6-2* in control conditions (0 MPa) or after 15 min of a −0.75-MPa treatment with (+) or without (−) Lyso-PS pretreatment. (**F**) DHE fluorescence quantification in *fer-4*, *fer-5*, PSS1ox1, and the crosses *fer-4*xPSS1ox1 and *fer-5* xPSS1ox1 in control (0 MPa) or treatment (−0.75 MPa) conditions. (**G**) DHE fluorescence quantification of mCit-ROP6gCA and *fer-4*x mCit-ROP6gCA in control condition (0 MPa) or after 15 min of a −0.75-MPa treatment with (+) or without (−) Lyso-PS pretreatment. (**H**) Confocal micrographs of Col-0 and *fer-4* cotyledon pavement cells revealed with propidium iodide, with or without Lyso-PS, and images of the *fer-4*xPSS1ox1 cross. The respective quantification of the pavement cell circularity index is shown (**I** and **J**). The closer the values to 1, the more circular the cells (J). Arrowheads show PM labeling. Error bars correspond to a confidence interval at 95%. According to ANOVA followed by Tukey test, letters indicate significant differences among means (*P* < 0.01). For (B) and (D), *n* > 7; for (E), (F), (G), and (I), *n* > 12 from at least two independent biological replicates. Scale bars, 20 μm (A and H) and 10 μM (C).

The tight link between PS nanodomains and ROP signaling has been recently uncovered. ROP6 is interacting with PM anionic lipids through lysine residues present in its hyper-variable tail (*6*). Genetic depletion of PS, one of the PM anionic lipids, induces a weaker retention of ROP6 in PS nanodomains (*6*). This loss of ROP6 retention within nanodomains was associated to a loss of ROP6-dependent auxin signaling. In *fer-4*, the total quantity of PS remains comparable to that in WT plants, but PS localization changes with relatively less PS at the PM together with a decreased density of PS-containing nanodomains. As observed in *pss1-3*, ROP6 nanodomains are still formed in *fer-4* after cell stimulation. However, ROP6 molecular diffusion is affected and stays high after osmotic stimulation. This suggests that PS organization at the PM participates in ROP6 immobility, likely through loss of interaction with ROP6's lysine residues, and consequently compromising osmotically induced ROS production.

The FER pathway affects PS accumulation/organization at the PM but without strong changes in terms of PS quantity in the plants. RALF23 behaves like an activator, since short-term treatment induces PS accumulation at the PM and conversely *fer-4*

shows a PS depletion. Long-term RALF23 treatment recapitulates the effect of FER loss of function on PS localization, ROS accumulation, and ROP6 dynamic. Therefore, it is possible, that upon its binding RALF23, FER is depleted from the PM by endocytosis, as it was describe for RALF1 treatment (*51*). However, how FER could regulate PS localization is currently unknown, as we do not know how PS gets to the PM. In yeast and mammalian cells, PS targeting is mediated at least for a part through ER/PM contact sites (*52*). Oxysterol-binding proteins transfer PS from the ER to the PM (*53*, *54*). Among others, they could be a target of FER activity to regulate PS nanodomains at the PM and/or PM/TGN partitioning. Because lipid exchanges between compartments is also achieved by vesicular trafficking, it could explain how overexpression of *PSS1* or exogenous application of lyso-lipids can complement *fer* phenotype, e.g., by passing ER/PM lipid transfer.

The role of PS on ROP signaling might be extendable to other ROP isoforms (*55*). While ROP single mutants have only a limited role on the pavement cell shape, multiple ROP mutants, overexpression of dominant negative or constitutively active ROPs, show much stronger phenotypes (*27*, *46*, *47*, *56*). Our

ability to show that PS is a limiting factor for pavement cell morphogenesis in FER loss of function suggests that PS nanodomains are also needed for other ROP isoforms mediating signaling through other types of ROP effectors, e.g., RIC1/Katanin (46, 47). It will be interesting to extend our model to pollen tube, since FER/ROP signaling regulates also RBOH-dependent ROS production (57). However, fer-4's defect in PTI signaling or auxin-induced root hair elongation is not recovered with exogenous supply of or genetic PS complementation, underlining the complexity of the pathways downstream of FER.

FER ligand binding is happening in the cell apoplast. Especially, LRXs constitute a physical link between the cell wall (via the extensin domain) and RALF peptides. LRX-RALF binding has been proposed to be regulated by the pH and redox potential of the cell wall, allowing transient dissociation of the RALF peptides that could be later perceived by FER (32). While the exact mechanistic framework of FER activation is still not fully understood, several examples in the literature suggest that FER responses are linked to cell wall status perception (18, 19, 58). As we found here that FER signaling regulates PS targeting and nanodomain formation, we think that cell wall physico-chemical status could be translated at the level of the PM by changing anionic lipid organization. This information is in turn used to modulate cell signaling events, such as ROP GTPase signaling. Thus, our work points to a new mechanism coupling physico-chemical stimulation to cell signaling.

MATERIALS AND METHODS

Plant material and growth

Arabidopsis thaliana ecotype Colombia (Col-0) was used as WT control. Following lines were previously published: *fer-4* (16), *fer-5* (14), *rop6-2*xmCit-ROP6gCA, p35S:GFP-ROP6 (5), UBQ10prom::mCitrine-2xPASS(NASC# N2107781), *pss1-3* (38), UBQ10prom::mCitrine-2xPH^{EVECTIN}(NASC# N2107779), UBQ10prom::mCitrine-C2^{LACT} (NASC#N2107347), and PSS1ox1(UBQ10prom::PSS1-mCitrine) (38). Crosses *fer-4*xprom-ROP6:mCitrine-ROP6-CA, *fer-5*xpromROP6:mCitrine-ROP6-CA, *fer-4*x2xPH^{EVECTIN}, *fer-5*x2xPH^{EVECTIN}, *fer-4*xC2^{LACT}, *fer-5*xC2^{LACT}, *fer-4*xPSS1ox1, and *fer-5*xPSS1ox1 were done in this study. Plants were stratified for 2 days at 4°C and grown vertically on 0.8% agar type E plates containing half-strength Murashige and Skoog (½ MS) medium supplemented with 1% (w/v) sucrose and 2.5 mM MES-KOH (pH 6) for 5 days at 22°C in a 16-hour light/8-hour dark cycle with 70% relative humidity and a light intensity of 200 µmol m^{-2} s^{-1}.

ROS quantification in root cells

The ROS quantification assay is as described in (4, 5). Briefly, to quantify the ROS production, 5 µM dihydroethidium (DHE) dye was used. Five-day-old plantlets were incubated in MS/2 liquid media to rest for 30 min and then transferred into 300 mM sorbitol (−0.75 MPa) for 15 min, 1 µM RALF23 (ATRRYISYGALRRN-TIPCSRRGASYYNCRRGAQANPYSRGCSAITRCRRS) for an hour, or 1 µM flg22 (QRLSTGSRINSAKDDAAGLQIA) for 30 min. Observations were performed at the transitional zone between the elongation and differentiation zone with an inverted fluorescent microscope Zeiss, 20× objective, using wavelength filter of 512/25 nm of the microscope lumencor with emission filter of 600/50 nm. The exposure time was 500 ms. Images were acquired using a charge coupled device (CDD) camera (Cooled SNAP HQ, Photometric), controlled by the fluorescence Ratio Imaging Software (MetaFluor).

Quantification of flg22-triggered ROS production in leaf discs

ROS assays were performed as previously described (59) with minor modification. Using a biopsy punch, at least eight leaf disks (4 mm in diameter) per genotype and condition were sampled on 5-week-old Arabidopsis plant leaves grown in short-day conditions and incubated overnight in a 96-well plate containing H$_2$O. The next day, the water was replaced by a solution containing 1 µM L-012 (Wako Pure Chemical Industries), peroxidase (20 µg ml^{-1}), and 100 nM flg22 (QRLSTGSRINSAKDDAAGLQIA). Luminescence was measured over 1 hour following elicitation or mock treatment using a Mithras LB 940 luminometer (Berthold Technologies). Total light unit production was calculated as the sum of photon counts measured over 1 hour postelicitation. For Lyso-PS complementation assays, eight leaf discs per treatment and genotype were collected in 96-well plates containing water and incubated overnight. The following day, the water was replaced by 75 µl of solution containing or not 50 µM Lyso-PS. Leaf discs were incubated further for 1 hour before adding 75 µl of a solution containing horseradish peroxidase (HRP; 40 µg/ml), 2 µM L-O12, and 200 nM flg22 (final concentration of 20 µg/ml HRP, 1 µM L-O12, and 100 nM flg22).

Subcellular and phenotype complementation with lysophospholipids

For complementation of the osmotically induced ROS, *fer-4* and *fer-5* were treated with Lyso-PS or LysoPA (54 µM, 1 hour) before imaging. For complementation of the subcellular localization PS sensors mCitrine-2xPH^{EVECTIN} and C2^{LACT} introgressed or not in *fer-4* or *fer-5* were treated with Lyso-PS or Lyso-PA (54 µM, 1 hour). PA sensor mCITRINE-2xPASS was concomitantly treated with 1 µM FIPI and lyso-PA (54 µM, 1 hour).

Western blot

Tissues from 5-day-old mCitrine-ROP6-CA, *fer-4*xmCitrine-ROP-CA, and *fer-5*xmCitrine-ROP6-CA were grinded with liquid nitrogen and resuspended in powder (1 ml/g) of radioimmunoprecipitation assay extraction buffer [150 mM NaCl, 50 mM tris-HCl (pH 8), 0.1% SDS, 0.5% Na deoxycholate, 1% Triton X-100, 2 mM leupeptin, 1 mM phenylmethylsulfonyl fluoride, and 5 mM dithiothreitol]. α-GFP-HRP (Miltenyi, 130-091-833) antibody for Western blot was diluted in blocking solution (1% bovine serum albumin in 0.1% Tween 20 and phosphate-buffered saline) at 1:2000. Total protein quantity was revealed with Coomassie blue stain.

Confocal laser scanning microscopy

Signal from the mCitrine-ROP6gCA, *fer-4*xmCitrine-ROP6gCA, *fer-5*xmCitrine-ROP6gCA, mCitrine-2PH^{EVECTIN}, mCitrine-C2^{LACT}, *fer-4*2PH^{EVECTIN}, *fer-5*2PH^{EVECTIN}, *fer-4*xC2^{LACT}, and *fer-5*xC2^{LACT} was imaged with a Leica SP8 microscope with a 40×/1.1 water objective. Argon laser (514 nm) was used, and fluorescence emission was collected at 530 to 560 nm for mCitrine-tagged lines. To quantify the PM/intracellular ratio on PS biosensors and mCitROP6gCA, we calculated and analyzed the "ratio plasma membrane/intracellular fluorescence intensity". This corresponds to the ratio between the fluorescence intensity (Mean Grey

Value function of Fiji software) measured along the PM region and four elliptical ROIs inside the cell (cytosol and intracellular compartments).

TIRF microscopy

For cluster density analysis of mCitrine-C2^{LACT}, fer-4xmCitrine-C2^{LACT}, and GFP-ROP6, in either resting conditions or treated with sorbitol, RALF23 or Lyso-PS, TIRF microscopy was done using the same inverted Zeiss microscope as for sptPALM (see the next section). One hundred images were acquired with 50-ms exposure time at 50 gains, with 488-nm excitation and 530/50-nm emission. From the 100 acquired images, an average intensity projection was computed. Segmentation of nanodomains was performed on the basis of the fluorescence signal from the average image using Machine Learning algorithm (60).

Single-particle tracking photoactivated localization microscopy

sptPALM experiments were carried out according to (43). Briefly, root cells were observed with a homemade TIRF microscope equipped with an electron-multiplying charge-coupled device camera (Andor iXON XU_897) and a 100× numerical aperture = 1.46 oil plan-apochromat objective (Zeiss). The laser angle was adjusted manually so that the generation of the evanescence waves gives a maximum signal-to-noise ratio when imaging the cell membrane close to the coverslip. The activation of the photo-convertible tagged mEOS-ROP6 was done by a low-intensity illumination at 405 nm (OBIS LX 50 mW; Coherent), and 561 nm (SAPPHIRE 100 mW; Coherent) emission combined with a 600/50 (Chroma) emission filter was used for image acquisition. Ten thousand images were recorded per ROI and streamed into a LabVIEW software (National Instruments) at 20-ms exposure time. Ten to 20 cells per were analyzed out of three biological replicates.

Single-particle tracking and Vonoroï tessellation

Individual single molecules were localized and tracked using the MTT software (61). Dynamic properties of single emitters in root cells were then inferred from the tracks using a homemade analysis software written in MATLAB (The MathWorks) (43). From each track, the diffusion coefficient D was then calculated by fitting the mean squared displacement (MSD) curve accordingly to (43). For the clustering analysis, the positions returned by MTT of each mEOS detection were used as input to the SR-Tesseler software (62). Correction for multiple detection of the same emitter was made on the basis of recommendation from (62). The local densities of each track were calculated as the invert of their minimal surface. Then, nanocluster size, relative number of ROP6 molecules in nanodomains, and density of nanoclusters were calculated after defining ROI where the local density was 50 times higher than the average. Only ROIs with at least 25 detections were considered.

Lipid extraction and lipid quantification

Five-day-old Col-0, fer-4, and fer-5 plants (0.1 to 1 g fresh weight) were collected in glass tubes; 2 ml of preheated isopropanol was added, and tubes were heated at 70°C for 20 min to inhibit phospholipase D activity. Six milliliters of chloroform/methanol 2/1 (v/v) was added, and lipid extraction was completed at room temperature. The organic phases were transferred to new glass tubes. Then, 1.5 ml

of H$_2$O was added to the organic phases, and tubes were vortexed and centrifuged at 2000 rpm; the organic phases were transferred to new glass tubes and evaporated, and the lipids were resuspended in the appropriate volume of chloroform/methanol 2/1 (v/v) to obtain the same concentration according to the initial seedlings fresh weight. Lipid separation and quantification were performed as described by (38).

For the analysis of phospholipids by liquid chromatography–tandem mass spectrometry (LC-MS/MS), lipid extracts were dissolved in 100 μl of eluent A (methanol/water 6/4 + 5 mM ammonium formate + 0.1% formic acid) containing synthetic internal lipid standards (PS 17:0/17:0; PE 17:0/17:0; Phosphatidylinositol (PI) 17:0/14:1, and PC 17:0/14:1 from Avanti Polar Lipids). LC-MS/MS (multiple reaction monitoring mode) analyses were performed with a model QTRAP 500 (ABSciex) mass spectrometer coupled to a liquid chromatography system (1290 Infinity II, Agilent). Analyses were performed in the negative (PS, PS, and PI) and positive (PC) modes with fast polarity switching (50 ms); mass spectrometry instrument parameters were as follows: turbo V source temperature (TEM) was set at 400°C; curtain gas (CUR) was nitrogen set at 30 psi; the nebulizing gas (GS1) was nitrogen set at 40 psi; the drying gas (GS2) was nitrogen set at 50 psi and the ion spray voltage (IS) was set at −4500 or +5500 V; and the declustering potential was adjusted between −160 and − 85 V or set at +35 V. The collision gas was also nitrogen; collision energy varied from −48 to −62 eV and +37 eV on a compound-dependent basis. Reverse-phase separations were performed at 40°C on a Supercolsil ABZ plus 2.1 mm by 100 mm column with 120-Å pore size and 3-μm particles (Supelco). The gradient elution program was as follows: 0 min, 20% B (isopropanol/methanol 8/2 + 5 mM ammonium formate + 0.1%formic acid); 10 min, 50% B; 54 min, 85% B. The flow rate was set at 0.20 ml/min, and 5 ml of sample volumes was injected. The areas of LC peaks were determined using MultiQuant software (version 2.1; ABSciex) for relative phospholipid quantification. Quantification of molecular phospholipid species was performed on three independent samples for Col-0, fer-4, and fer-5.

Cotyledon and pavement cells

Plantlets were grown on (½ MS) medium supplemented with 1% (w/v) sucrose and 2.5 mM MES-KOH (pH 6) media for 3 days and, if required, then transferred to media supplemented or not by Lyso-PS or Lyso-PA (2.2 μM) for additional three more days. Pavement cells were revealed with propidium iodide (1 mg/ml) stained for 20 min and then washed in media for 5 min. They were imaged with a SP8 (Leica) with a 40×/1.1 water objective. Excitation was set at 514 nm, and light was collected between 600 and 640 nm. Circularity index was measured with ImageJ tool: shape description. To quantify cotyledon circularity index, cotyledons from 7-day-old plantlets were pulled off and imaged with a macroscope (Axizoom, Zeiss).

Gravistimulation experiment

Col-0, fer-4, PSS1ox1, and fer-4xPSS1ox1 were grown for 4 days on regular ½ MS media [supplemented with 1% (w/v) sucrose and 2.5 mM MES-KOH (pH 5.8)] in short-day conditions at 21°C. On the fourth day, plants were transferred in a new plate containing the same media, and the primary root was delicately stretched. Gravistimulation was performed by a 90° left rotation of the whole plate. After 6 hours, plates were imaged with a scanner at 800 dot per inch

(dpi) 16 bits. Images were analyzed in ImageJ to determine the angle formed between the root tip and the primary root highlighting the gravitropic response.

Auxin-induced root hair elongation

Plants were grown for 5 days on regular ½ MS supplemented with 125 nM naphthaleneacetic acid and imaged with an Axiozom (Zeiss).

Statistical analysis

In each experiment, 8 to 10 cells were studied from five to seven different seedlings. All experiments were independently repeated two to three times. Each cell was analyzed individually to include the maximum of the biological variation. Data are expressed as mean ± 95% confidence interval. Analysis of variance (ANOVA) followed by Tukey test was done, and letters indicate significant differences among means ($P < 0.001$). Statistical analysis such as ANOVA followed by a Tukey post hoc test and t test was done in GraphPad Prism.

Supplementary Materials

This PDF file includes:
Figs. S1 to S6

View/request a protocol for this paper from *Bio-protocol*.

REFERENCES AND NOTES

1. J. Lamers, T. van der Meer, C. Testerink, How plants sense and respond to stressful environments. *Plant Physiol.* **182**, 1624–1635 (2020).
2. R. C. Nongpiur, S. L. Singla-Pareek, A. Pareek, The quest for osmosensors in plants. *J. Exp. Bot.* **71**, 595–607 (2020).
3. Y. Leshem, L. Seri, A. Levine, Induction of phosphatidylinositol 3-kinase-mediated endocytosis by salt stress leads to intracellular production of reactive oxygen species and salt tolerance. *Plant J.* **51**, 185–197 (2007).
4. A. Martinière, J. B. Fiche, M. Smokvarska, S. Mari, C. Alcon, X. Dumont, K. Hematy, Y. Jaillais, M. Nollmann, C. Maurel, Osmotic stress activates two reactive oxygen species pathways with distinct effects on protein nanodomains and diffusion. *Plant Physiol.* **179**, 1581–1593 (2019).
5. M. Smokvarska, C. Francis, M. P. Platre, J.-B. Fiche, C. Alcon, X. Dumont, P. Nacry, V. Bayle, M. Nollmann, C. Maurel, Y. Jaillais, A. Martiniere, A plasma membrane nanodomain ensures signal specificity during osmotic signaling in plants. *Curr. Biol.* **30**, 4654–4664.e4 (2020).
6. M. P. Platre, V. Bayle, L. Armengot, J. Bareille, M. D. M. Marquès-Bueno, A. Creff, L. Maneta-Peyret, J.-B. Fiche, M. Nollmann, C. Miège, P. Moreau, A. Martinière, Y. Jaillais, Developmental control of plant Rho GTPase nano-organization by the lipid phosphatidylserine. *Science* **364**, 57–62 (2019).
7. H. J. G. Meijer, N. Divecha, H. van den Ende, A. Musgrave, T. Munnik, Hyperosmotic stress induces rapid synthesis of phosphatidyl-D-inositol 3,5-bisphosphate in plant cells. *Planta* **208**, 294–298 (1999).
8. T. Munnik, H. J. G. Meijer, B. Ter Riet, H. Hirt, W. Frank, D. Bartels, A. Musgrave, Hyperosmotic stress stimulates phospholipase D activity and elevates the levels of phosphatidic acid and diacylglycerol pyrophosphate. *Plant J.* **22**, 147–154 (2000).
9. L. Vaahtera, J. Schulz, T. Hamann, Cell wall integrity maintenance during plant development and interaction with the environment. *Nat. Plants.* **5**, 924–932 (2019).
10. Y. Rui, J. R. Dinneny, A wall with integrity: Surveillance and maintenance of the plant cell wall under stress. *New Phytol.* **225**, 1428–1439 (2020).
11. S. Wolf, Cell wall signaling in plant development and defense. *Annu. Rev. Plant Biol.* **73**, 323–353 (2022).
12. S. Zhu, Q. Fu, F. Xu, H. Zheng, F. Yu, New paradigms in cell adaptation: Decades of discoveries on the CrRLK1L receptor kinase signalling network. *New Phytol.* **232**, 1168–1183 (2021).
13. J.-M. Escobar-Restrepo, N. Huck, S. Kessler, V. Gagliardini, J. Gheysselinck, W.-C. Yang, U. Grossniklaus, The FERONIA receptor-like kinase mediates male-female interactions during pollen tube reception. *Science* **317**, 656–660 (2007).
14. Q. Duan, D. Kita, C. Li, A. Y. Cheung, H.-M. Wu, FERONIA receptor-like kinase regulates RHO GTPase signaling of root hair development. *Proc. Natl. Acad. Sci. U.S.A.* **107**, 17821–17826 (2010).
15. F. Yu, L. Qian, C. Nibau, Q. Duan, D. Kita, K. Levasseur, X. Li, C. Lu, H. Li, C. Hou, L. Li, B. B. Buchanan, L. Chen, A. Y. Cheung, D. Li, S. Luan, FERONIA receptor kinase pathway suppresses abscisic acid signaling in Arabidopsis by activating ABI2 phosphatase. *Proc. Natl. Acad. Sci. U.S.A.* **109**, 14693–14698 (2012).
16. M. Haruta, G. Sabat, K. Stecker, B. B. Minkoff, M. R. Sussman, A peptide hormone and its receptor protein kinase regulate plant cell expansion. *Science* **343**, 408–411 (2014).
17. M. Stegmann, J. Monaghan, E. Smakowska-Luzan, H. Rovenich, A. Lehner, N. Holton, Y. Belkhadir, C. Zipfel, The receptor kinase FER is a RALF-regulated scaffold controlling plant immune signaling. *Science* **355**, 287–289 (2017).
18. W. Feng, D. Kita, A. Peaucelle, H. N. Cartwright, V. Doan, Q. Duan, M.-C. Liu, J. Maman, L. Steinhorst, I. Schmitz-Thom, R. Yvon, J. Kudla, H.-M. Wu, A. Y. Cheung, J. R. Dinneny, The FERONIA receptor kinase maintains cell-wall integrity during salt stress through Ca^{2+} signaling. *Curr. Biol.* **28**, 666–675.e5 (2018).
19. C. Zhao, O. Zayed, Z. Yu, W. Jiang, P. Zhu, C.-C. Hsu, L. Zhang, W. A. Tao, R. Lozano-Durán, J.-K. Zhu, Leucine-rich repeat extensin proteins regulate plant salt tolerance in *Arabidopsis*. *Proc. Natl. Acad. Sci. U.S.A.* **115**, 13123–13128 (2018).
20. K. Dünser, S. Gupta, A. Herger, M. I. Feraru, C. Ringli, J. Kleine-Vehn, Extracellular matrix sensing by FERONIA and Leucine-Rich Repeat Extensins controls vacuolar expansion during cellular elongation in *Arabidopsis thaliana*. *EMBO J.* **38**, e100353 (2019).
21. C. Liu, L. Shen, Y. Xiao, D. Vyshedsky, C. Peng, X. Sun, Z. Liu, L. Cheng, H. Zhang, Z. Han, J. Chai, H.-M. Wu, A. Y. Cheung, C. Li, Pollen PCP-B peptides unlock a stigma peptide-receptor kinase gating mechanism for pollination. *Science* **372**, 171–175 (2021).
22. A. Malivert, Ö. Erguvan, A. Chevallier, A. Dehem, R. Friaud, M. Liu, M. Martin, T. Peyraud, O. Hamant, S. Verger, FERONIA and microtubules independently contribute to mechanical integrity in the Arabidopsis shoot. *PLOS Biol.* **19**, e3001454 (2021).
23. Y. Song, A. J. Wilson, X.-C. Zhang, D. Thoms, R. Sohrabi, S. Song, Q. Geissmann, Y. Liu, L. Walgren, S. Y. He, C. H. Haney, FERONIA restricts Pseudomonas in the rhizosphere microbiome via regulation of reactive oxygen species. *Nat. Plants.* **7**, 644–654 (2021).
24. W. Tang, W. Lin, X. Zhou, J. Guo, X. Dang, B. Li, D. Lin, Z. Yang, Mechano-transduction via the pectin-FERONIA complex activates ROP6 GTPase signaling in Arabidopsis pavement cell morphogenesis. *Curr. Biol.* **32**, 508–517.e3 (2021).
25. S. Zhong, L. Li, Z. Wang, Z. Ge, Q. Li, A. Bleckmann, J. Wang, Z. Song, Y. Shi, T. Liu, L. Li, H. Zhou, Y. Wang, L. Zhang, H.-M. Wu, L. Lai, H. Gu, J. Dong, A. Y. Cheung, T. Dresselhaus, L.-J. Qu, RALF peptide signaling controls the polytubey block in *Arabidopsis*. *Science* **375**, 290–296 (2022).
26. Q. Duan, D. Kita, E. A. Johnson, M. Aggarwal, L. Gates, H.-M. Wu, A. Y. Cheung, Reactive oxygen species mediate pollen tube rupture to release sperm for fertilization in Arabidopsis. *Nat. Commun.* **5**, 3129 (2014).
27. W. Lin, W. Tang, X. Pan, A. Huang, X. Gao, C. T. Anderson, Z. Yang, Arabidopsis pavement cell morphogenesis requires FERONIA binding to pectin for activation of ROP GTPase signaling. *Curr. Biol.* **32**, 497–507.e4 (2021).
28. Y. Xiao, M. Stegmann, Z. Han, T. A. DeFalco, K. Parys, L. Xu, Y. Belkhadir, C. Zipfel, J. Chai, Mechanisms of RALF peptide perception by a heterotypic receptor complex. *Nature* **572**, 270–274 (2019).
29. A. Abarca, C. M. Franck, C. Zipfel, Family-wide evaluation of RAPID ALKALINIZATION FACTOR peptides. *Plant Physiol.* **187**, 996–1010 (2021).
30. C. Li, F.-L. Yeh, A. Y. Cheung, Q. Duan, D. Kita, M.-C. Liu, J. Maman, E. J. Luu, B. W. Wu, L. Gates, M. Jalal, A. Kwong, H. Carpenter, H.-M. Wu, Glycosylphosphatidylinositol-anchored proteins as chaperones and co-receptors for FERONIA receptor kinase signaling in Arabidopsis. *eLife* **4**, e06587 (2015).
31. P. Liu, M. Haruta, B. B. Minkoff, M. R. Sussman, Probing a plant plasma membrane receptor kinase's three-dimensional structure using mass spectrometry-based protein footprinting. *Biochemistry* **57**, 5159–5168 (2018).
32. S. Moussu, C. Broyart, G. Santos-Fernandez, S. Augustin, S. Wehrle, U. Grossniklaus, J. Santiago, Structural basis for recognition of RALF peptides by LRX proteins during pollen tube growth. *Proc. Natl. Acad. Sci. U.S.A.* **117**, 7494–7503 (2020).
33. A. Herger, S. Gupta, G. Kadler, C. M. Franck, A. Boisson-Dernier, C. Ringli, Overlapping functions and protein-protein interactions of LRR-extensins in Arabidopsis. *PLOS Genet.* **16**, e1008847 (2020).
34. J. Chen, F. Yu, Y. Liu, C. Du, X. Li, S. Zhu, X. Wang, W. Lan, P. L. Rodriguez, X. Liu, D. Li, L. Chen, S. Luan, FERONIA interacts with ABI2-type phosphatases to facilitate signaling cross-talk between abscisic acid and RALF peptide in *Arabidopsis*. *Proc. Natl. Acad. Sci. U.S.A.* **113**, E5519–E5527 (2016).
35. J. Gronnier, C. M. Franck, M. Stegmann, T. A. DeFalco, A. Abarca, M. Von Arx, K. Dünser, W. Lin, Z. Yang, J. Kleine-Vehn, C. Ringli, C. Zipfel, Regulation of immune receptor kinase

plasma membrane nanoscale organization by a plant peptide hormone and its receptors. *eLife* **11**, e74162 (2022).

36. L. Wang, T. Yang, Q. Lin, B. Wang, X. Li, S. Luan, F. Yu, Receptor kinase FERONIA regulates flowering time in *Arabidopsis*. *BMC Plant Biol.* **20**, 26 (2020).

37. S. Zhu, J. Martínez Pacheco, J. M. Estevez, F. Yu, Autocrine regulation of root hair size by the RALF-FERONIA-RSL4 signaling pathway. *New Phytol.* **227**, 45–49 (2020).

38. M. P. Platre, L. C. Noack, M. Doumane, V. Bayle, M. L. A. Simon, L. Maneta-Peyret, L. Fouillen, T. Stanislas, L. Armengot, P. Pejchar, M.-C. Caillaud, M. Potocký, A. Čopič, P. Moreau, Y. Jaillais, A combinatorial lipid code shapes the electrostatic landscape of plant endo-membranes. *Dev. Cell.* **45**, 465–480.e11 (2018).

39. M. L. A. Simon, M. P. Platre, M. M. Marquès-Bueno, L. Armengot, T. Stanislas, V. Bayle, M.-C. Caillaud, Y. Jaillais, A PtdIns(4)P-driven electrostatic field controls cell membrane identity and signalling in plants. *Nat. Plants* **2**, 16089 (2016).

40. Y. Uchida, J. Hasegawa, D. Chinnapen, T. Inoue, S. Okazaki, R. Kato, S. Wakatsuki, R. Misaki, M. Koike, Y. Uchiyama, S. Iemura, T. Natsume, R. Kuwahara, T. Nakagawa, K. Nishikawa, K. Mukai, E. Miyoshi, N. Taniguchi, D. Sheff, W. I. Lencer, T. Taguchi, H. Arai, Intracellular phosphatidylserine is essential for retrograde membrane traffic through endosomes. *Proc. Natl. Acad. Sci. U.S.A.* **108**, 15846–15851 (2011).

41. J. Chung, F. Torta, K. Masai, L. Lucast, H. Czapla, L. B. Tanner, P. Narayanaswamy, M. R. Wenk, F. Nakatsu, P. De Camilli, PI4P/phosphatidylserine countertransport at ORP5- and ORP8-mediated ER-plasma membrane contacts. *Science* **349**, 428–432 (2015).

42. E. Hosy, A. Martinière, D. Choquet, C. Maurel, D.-T. Luu, Super-resolved and dynamic imaging of membrane proteins in plant cells reveal contrasting kinetic profiles and multiple confinement mechanisms. *Mol. Plant* **8**, 339–342 (2015).

43. V. Bayle, J.-B. Fiche, C. Burny, M. P. Platre, M. Nollmann, A. Martinière, Y. Jaillais, Single-particle tracking photoactivated localization microscopy of membrane proteins in living plant tissues. *Nat. Protoc.* **16**, 1600–1628 (2021).

44. K. Maeda, K. Anand, A. Chiapparino, A. Kumar, M. Poletto, M. Kaksonen, A.-C. Gavin, Interactome map uncovers phosphatidylserine transport by oxysterol-binding proteins. *Nature* **501**, 257–261 (2013).

45. J. Moser von Filseck, S. Vanni, B. Mesmin, B. Antonny, G. Drin, A phosphatidylinositol-4-phosphate powered exchange mechanism to create a lipid gradient between membranes. *Nat. Commun.* **6**, 6671 (2015).

46. X. Pan, L. Fang, J. Liu, B. Senay-Aras, W. Lin, S. Zheng, T. Zhang, J. Guo, U. Manor, J. Van Norman, W. Chen, Z. Yang, Auxin-induced signaling protein nanoclustering contributes to cell polarity formation. *Nat. Commun.* **11**, 3914 (2020).

47. Y. Fu, Y. Gu, Z. Zheng, G. Wasteneys, Z. Yang, Arabidopsis interdigitating cell growth requires two antagonistic pathways with opposing action on cell morphogenesis. *Cell* **120**, 687–700 (2005).

48. C. M. Franck, J. Westermann, A. Boisson-Dernier, Plant malectin-like receptor kinases: From cell wall integrity to immunity and beyond. *Annu. Rev. Plant Biol.* **69**, 301–328 (2018).

49. Y. Yu, D. Chakravorty, S. M. Assmann, The G Protein β-Subunit, AGB1, interacts with FERONIA in RALF1-regulated stomatal movement. *Plant Physiol.* **176**, 2426–2440 (2018).

50. S. A. Kessler, H. Shimosato-Asano, N. F. Keinath, S. E. Wuest, G. Ingram, R. Panstruga, U. Grossniklaus, Conserved molecular components for pollen tube reception and fungal invasion. *Science* **330**, 968–971 (2010).

51. M. Yu, R. Li, Y. Cui, W. Chen, B. Li, X. Zhang, Y. Bu, Y. Cao, J. Xing, P. K. Jewaria, X. Li, R. P. Bhalerao, F. Yu, J. Lin, The RALF1-FERONIA interaction modulates endocytosis to mediate control of root growth in *Arabidopsis*. *Development* **147**, dev189902 (2020).

52. L. Scorrano, M. A. De Matteis, S. Emr, F. Giordano, G. Hajnóczky, B. Kornmann, L. L. Lackner, T. P. Levine, L. Pellegrini, K. Reinisch, R. Rizzuto, T. Simmen, H. Stenmark, C. Ungermann, M. Schuldiner, Coming together to define membrane contact sites. *Nat. Commun.* **10**, 1287 (2019).

53. B. Antonny, J. Bigay, B. Mesmin, The oxysterol-binding protein cycle: Burning off PI(4)P to transport cholesterol. *Annu. Rev. Biochem.* **87**, 809–837 (2018).

54. G. A. Dubois, Y. Jaillais, Anionic phospholipid gradients: An uncharacterized frontier of the plant endomembrane network. *Plant Physiol.* **185**, 577–592 (2021).

55. M. Smokvarska, Y. Jaillais, A. Martinière, Function of membrane domains in rho-of-plant signaling. *Plant Physiol.* **185**, 663–681 (2021).

56. Y. Fu, T. Xu, L. Zhu, M. Wen, Z. Yang, A ROP GTPase Signaling Pathway Controls Cortical Microtubule Ordering and Cell Expansion in Arabidopsis. *Curr. Biol.* **19**, 1827–1832 (2009).

57. L. Zhang, J. Huang, S. Su, X. Wei, L. Yang, H. Zhao, J. Yu, J. Wang, J. Hui, S. Hao, S. Song, Y. Cao, M. Wang, X. Zhang, Y. Zhao, Z. Wang, W. Zeng, H.-M. Wu, Y. Yuan, X. Zhang, A. Y. Cheung, Q. Duan, FERONIA receptor kinase-regulated reactive oxygen species mediate self-incompatibility in *Brassica rapa*. *Curr. Biol.* **31**, 3004–3016.e4 (2021).

58. H.-W. Shih, N. D. Miller, C. Dai, E. P. Spalding, G. B. Monshausen, The receptor-like kinase FERONIA is required for mechanical signal transduction in arabidopsis seedlings. *Curr. Biol.* **24**, 1887–1892 (2014).

59. Y. Kadota, J. Sklenar, P. Derbyshire, L. Stransfeld, S. Asai, V. Ntoukakis, J. D. Jones, K. Shirasu, F. Menke, A. Jones, C. Zipfel, Direct regulation of the NADPH oxidase RBOHD by the PRR-associated kinase BIK1 during plant immunity. *Mol. Cell* **54**, 43–55 (2014).

60. S. Berg, D. Kutra, T. Kroeger, C. N. Straehle, B. X. Kausler, C. Haubold, M. Schiegg, J. Ales, T. Beier, M. Rudy, K. Eren, J. I. Cervantes, B. Xu, F. Beuttenmueller, A. Wolny, C. Zhang, U. Koethe, F. A. Hamprecht, A. Kreshuk, ilastik: Interactive machine learning for (bio)image analysis. *Nat. Methods.* **16**, 1226–1232 (2019).

61. A. Sergé, N. Bertaux, H. Rigneault, D. Marguet, Dynamic multiple-target tracing to probe spatiotemporal cartography of cell membranes. *Nat. Methods* **5**, 687–694 (2008).

62. F. Levet, E. Hosy, A. Kechkar, C. Butler, A. Beghin, D. Choquet, J.-B. Sibarita, SR-Tesseler: A method to segment and quantify localization-based super-resolution microscopy data. *Nat. Methods* **12**, 1065–1071 (2015).